# Applications for rotational seismic data

*Ohad Barak and Shuki Ronen*

## ABSTRACT

Seismic systems today record up to four components which provide the particle displacement and the pressure. The pressure is proportional to the divergence of the displacement. The curl of the displacements can be recorded using rotation sensors.

To evaluate the added information that would come from rotation sensors we use elastic modeling. In our synthetic data experiment, we predict the effect of a seabed scatterer on seven-component OBS data: three component geophones, three component rotation sensors and hydrophones.

The synthetic data comprises P-waves, S-waves and surface waves. We apply singular value decomposition in order to identify the polarization vectors for each wave type. Our evaluation is that the added information from rotation sensors is useful for identifying and separating surface waves from body waves.

Additionally, we use elastic modeling to predict how a change in rock-physics parameters affects the AVO curve of the rotational-motion components, and compare the response to a standard AVO obtained from the hydrophone component.

## INTRODUCTION

Four-component ocean-bottom seismic sensors are a combination of a hydrophone and three-component geophones that measure linear particle velocity. The hydrophone records pressure changes in the water, and is ideally coupled to the water. It picks up mostly P-waves. The geophones are coupled to the sea-bed, and record particle velocities related to all wave modes: P, S, and surface waves. The multiplicity of wave modes recorded by the geophones can be problematic for later seismic processing stages, which assume a single wave mode recording (i.e., imaging with P-wave or S-wave data only). It is therefore desirable to be able to separate different wave modes within the data.

The divergence of particle motion is a spatial derivative. If we knew the displacement values everywhere within the seismic volume, then we could calculate the divergence. However, receiver stations may be too sparse in relation to the seismic wavelengths to calculate the divergence, and, in any case, are always spread along a single surface (the sea bottom). The value of the divergence is not redundant even if we measure the three components of the displacement, since it can be used to detect

the propagation direction of the waves incident on the sea bottom (upward or downward). The pressure that the hydrophone records is proportional to the divergence of the particle displacements, and is therefore used for upgoing/downgoing wavefield separation.

Similar to the divergence, we can measure the rotation of particle motion by calculating the curl of the displacements. As with the divergence, curl is a spatial derivative operator, and insufficient sampling of the waves in the field can inhibit its direct calculation. However, a recently-proposed rotation sensor can be used to measure the rotation "in place". A rotation sensor measures the rotation rate (radians/unit time) of the ground at the receiver location. Similar to linear motion, the rotational motion has three components: roll, pitch and yaw. Figure 1 illustrates these motion components.

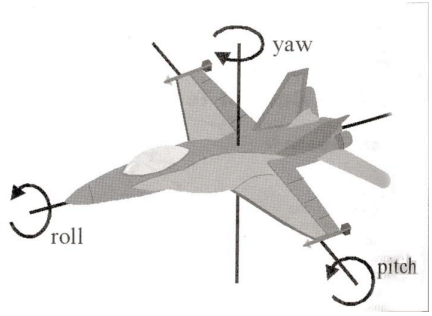


Figure 1: To know what an aircraft is doing, it is not sufficient to know its linear velocity but also the rotations. There are three components to the velocity, and in addition there are three components to the rotation: roll, pitch, and yaw. [**NR**]

There are implementations of rotational seismic recording for earthquake seismology (Lee et al., 2009) employing ring lasers. However, these instruments are large and expensive, and are therefore not applicable to exploration acquisition. There have also been attempts to record rotational seismic data with a "Rotaphone" - conventional geophones arranged along a circle (Brokesova and Malek, 2010). Newer technologies are currently under development to make rotational sensors a viable option for seismic acquisition systems. The USGS has recently tested a small number of rotation sensors at the Calpine geothermal power station near The Geysers in California. Chevron has conducted a small land survey that included rotational sensors, in order to evaluate the quality and the possible uses for such data.

Several authors have proposed applications for rotational seismic data (Brune et al., 2012; Muyzert et al., 2012; Edme et al., 2012). In this paper we propose two applications:

1. using rotational data for identifying and filtering surface waves, and
2. constructing converted-wave AVO curves, where the rotation data is a proxy for the reflected shear-wave energy.

## Linear versus rotational polarization

deMeersman et al. (2006) apply SVD on three-component geophone data in order to estimate the polarization direction of P-wave arrivals. Similarly, it is possible to apply SVD on 6-component data comprising a 3C geophone and a 3C rotation sensor. The resulting polarization vector indicates not only linear polarization, but also rotational polarization. The combination of linear and rotational polarization components provide an indication of the wave type. Body waves generate linear particle motion, and have a mostly linear polarization. Surface waves (Rayleigh, Scholte, Love) generate elliptical particle motion, and therefore cause a greater rotational deformation on a finite volume element. Therefore, they should be polarized more along a rotational axis than a linear axis.

We synthesized 3D ocean-bottom seismic data. To simulate seven-component acquisition, we recorded the pressure in the water just above the ocean-bottom, and the particle velocity and rotations at the water bottom. The data contains both body waves and surface waves. We then applied SVD to the seven components of specific arrivals, which we identified apriori as P, SV, SH, or Scholte waves. The scaled, orthogonal polarization vectors of these arrivals show how the waves are polarized in a seven-dimensional space comprising one pressure, three linear-motion and three rotational-motion axes.

## Rotational AVO for gas hydrates

Gas hydrates are a form of water crystal that have a specific structure, and which are stabilized by the inclusion of methane gas molecules. The presence of a gas hydrate saturated layer can be seen in some seismic data. The high impedance contrast between the gas hydrate layer and the underlying sediments creates a strong seismic signature known as a bottom simulating reflector (BSR).

Rock-physics models of gas hydrates, which connect density, porosity, effective pressure, mineralogy and pore-space saturation in marine sediments containing the hydrates to elastic properties have been developed (Ecker et al., 1997; Dvorkin and Nur, 1993). The micromechanical structure of the hydrate and the porosity of the sediment in which it forms will affect the level of hydrate saturation, and therefore the total amount of methane gas within those sediments.

Several rock physics models exist to describe the way the gas hydrate is included in the sediments. But the determination of which model is the best representation dependends on accurate acquisition of several material parameters: mineralogy, density, porosity and saturation. These properties can be measured using well logs, and can be compared to data acquired by seismic surveys. The information in P-wave reflections can be used to determine some of these parameters. However, the P-wave reflectivity is not very sensitive to the shear strength of the medium, which is the one parameter which very clearly separates gas hydrates from their typical sedimen-

tary surrounding. The wavefield curl is a proxy for the shear waves amplitude, and recording it can help in getting a better estimation of the host rock properties and the internal structure of hydrate sediments.

Utilizing the rock-physics models and data from a well logs near Blake Outer Ridge, where a hydrate layer is present, we constructed a 1.5D medium with effective elastic properties. We used elastic modeling to predict how a change in rock physics parameters would affect the AVO curve of the rotational-motion components recorded by rotation sensors, and compared the response to AVO obtained from the hydrophone component. We do not actually plot the AVO curve, but we do show a CMP gather obtained from a synthetic OBS experiment in a medium with a single flat hydrate layer, and therefore the amplitudes observed over offset are comparable to an AVO.

# THEORY

## Elastic wave propagation

The isotropic elastic wave equation has two state variables: the stress tensor and the particle velocity vector. The particle velocities are propagated by solving:

$$\partial_i \sigma_{ii} + \partial_j \sigma_{ij} + f_i(\mathbf{x}, t) = \rho \partial_t v_i, \tag{1}$$

where $\sigma_{ii}$ are the normal stresses, $\sigma_{ij}$ are the transverse stresses, $f_i$ is a particle velocity force function in direction $i$, $\mathbf{x}$ is the spatial source location operating at time $t$, $\rho$ is density and $v_i$ is the particle velocity in direction $i$. The stresses are propagated using the stress-displacement relation:

$$\begin{aligned} \partial_t \sigma_{ii} &= (\lambda + 2\mu)\partial_i v_i + \lambda \partial_j v_j + f^P(\mathbf{x}, t), \\ \partial_t \sigma_{ij} &= \mu \left( \partial_j v_i + \partial_i v_j \right), \end{aligned} \tag{2}$$

where $\lambda$ and $\mu$ are the Lamé elastic constants and $f^P$ is a pressure force function. The pressure force is added equally to the normal stresses to generate a P-wave source.

We use the staggered time grid methodology for elastic propagation (Virieux, 1986), in which the stresses and particle velocities are half a time-step apart. Equations 1 and 2 are solved in alternation during the propagation.

The divergence of particle displacements is proportional to the pressure in the medium, the proportion being the medium parameters. It is equal to the average of the normal stresses in the stress tensor:

$$P = \overline{\boldsymbol{\sigma}} = \frac{2}{3} \left( \lambda + \mu \right) \nabla \cdot \vec{\mathbf{u}}, \tag{3}$$

where $P$ is the pressure value and $\vec{\mathbf{u}}$ are the displacements. Pressure waves cause a volumetric deformation in the medium, and their value can therefore be extracted by using equation 3 on forward modeled wavefields. However, other wave types can also generate a volumetric deformation at free surfaces, as a result of the discontinuity of the stresses.

We define rotation as the first time derivative of the curl of displacements:

$$\vec{\mathbf{R}} = \partial_t \nabla \times \vec{\mathbf{u}}. \tag{4}$$

The curl operation results in the non-volumetric part of the deformation, i.e. the "shear" deformation. At a free surface, this deformation will cause a rotation. In an isotropic medium, the curl is associated with S-waves. However, at a free surface, both P-waves and surface waves will also generate non-volumetric deformation. The units we use for rotations in this paper are milliradians/second, while the units for particle velocity are millimeters/second.

## Singular value decomposition of seven-component data

Given a seven-component seismic dataset with a seismogram consisting of pressure $h(t)$, particle velocity $v_z(t)$, $v_x(t)$ and $v_y(t)$ recorded in the Z, X and Y directions, and rotation $r_z(t)$, $r_x(t)$ and $r_y(t)$ recorded in the Z, X and Y directions, we can constuct an Nx7 data matrix $\mathbf{D} = [h(t), v_z(t), v_x(t), v_y(t), r_z(t), r_x(t), r_y(t)]$. Each column is a recording of one component over a certain time window. SVD is a method of finding the waveform $\mathbf{u}_s$, magnitude $\sigma_s$, and polarization $\mathbf{v}_s$ of the signal that is present in the data $\mathbf{D}$. The SVD of the data $\mathbf{D}$ is given by

$$\mathbf{D} = \mathbf{U}\mathbf{\Lambda}\mathbf{V}^T, \tag{5}$$

where $\mathbf{D}$ is the product of the Nx7 matrix $\mathbf{U}$, the 7x7 diagonal matrix $\mathbf{\Lambda}$, and the transpose of the 7x7 matrix $\mathbf{V}$. The unit left and right singular vectors $\mathbf{u}_i$ and $\mathbf{v}_i$ are the seven column vectors of $\mathbf{U}$ and $\mathbf{V}$. The singular values $\sigma_i$ are the diagonal elements of $\mathbf{\Lambda}$. They are ordered such that $|\lambda_1|$ is the greatest and $|\lambda_7|$ the smallest.

The left and right singular vectors are mutually orthogonal, such that $\mathbf{U}^T\mathbf{U} = \mathbf{I}$ and $\mathbf{V}\mathbf{V}^T = \mathbf{I}$. An SVD therefore decomposes the data matrix into its orthogonal parts.

The right singular vectors $\mathbf{v}_i$ display the polarization of the data within a particular time window along the seven axes. We transpose and multiply the matrix $\mathbf{V}$ by the singular value matrix $\mathbf{\Lambda}$, to obtain the scaled polarization vectors:

$$\mathbf{s}_i = \sigma_i v_i^T. \tag{6}$$

## Hydrate inclusion models

Ecker et al. (1997) developed three different rock physics models for the inclusion of gas hydrates in porous sedimentary rock, and tested these models against well-log data and seismic data from the Blake Outer Ridge. These models are:

1. Hydrate is a part of the fluid in the pore-space
2. Hydrate is a part of the solid host rock
3. Hydrate cements the grains of the host rock

The models are illustrated in Figure 2. They pertain to loosely consolidated sedimentary rock, which is the case for the Blake Outer Ridge, near the passive continental margin offshore Eastern Florida. Each model produces a different estimate of the elastic moduli of the hydrate-containing sediment, as a function of porosity and saturation of the rock. We will deal only with the first and second inclusion models.

## Model 1 - Hydrate is part of fluid

When the hydrate is assumed to be part of the fluid, the fluid's bulk modulus and the solid's dry moduli are calculated separately, and then Gassmann's fluid substitution is used to saturate the rock. The fluid's modulus is an average of the water and the hydrate moduli:

$$K_f \;=\; [S_w \,/\, K_w \;+\; (1 - S_w) \,/\, K_h]^{-1}, \tag{7}$$

where $K_h$ is the bulk modulus of the hydrate, $K_w$ the bulk modulus of water and $S_w$ the water saturation. The solid's dry moduli are calculated using the modified Hashin-Shtrikman-Hertz-Mindlin theory (Dvorkin and Nur (1996)). For porosity below critical porosity ($\phi_c = 0.4$) the moduli are:

$$\begin{aligned}
K_{dry} &= \left[\frac{\phi/\phi_c}{K_{HM} \,+\, \frac{4}{3}\,G_{HM}} \,+\, \frac{1 \,-\, \phi/\phi_c}{K \,+\, \frac{4}{3}\,G_{HM}}\right]^{-1} \,-\, \frac{4}{3}\,G_{HM}, \\
G_{dry} &= \left[\frac{\phi/\phi_c}{G_{HM} + Z} \,+\, \frac{1 \,-\, \phi/\phi_c}{G \,+\, Z}\right]^{-1} - Z, \\
Z &= \frac{G_{HM}}{6}\,\left(\frac{9\,K_{HM} \,+\, 8\,G_{HM}}{K_{HM} \,+\, 2\,G_{HM}}\right),
\end{aligned} \tag{8}$$

where $K_{HM}$ and $G_{HM}$ are the Hertz-Mindlin effective moduli, $\phi$ is porosity and $\phi_c$ is the critical porosity.
The saturated moduli using Gassman's fluid substitution are:

$$\begin{aligned} K_{sat} &= K \frac{\phi\, K_{dry} - (1+\phi)\, K_f\, K_{dry}/K + K_f}{(1-\phi)\, K_f + \phi\, K - K_f\, K_{dry}/K}, \text{and} \\ G_{sat} &= G_{dry}. \end{aligned} \tag{9}$$

The elastic velocities $V_p$ and $V_s$ and the bulk density $\rho_B$ are then given by:

$$\begin{aligned} \rho_B &= (1-\phi)\, \rho_s + \phi\, \rho_f, \\ V_p &= \sqrt{(K_{sat} + \frac{4}{3} G_{sat})/\rho_B}, \\ V_s &= \sqrt{G_{sat}/\rho_B}, \end{aligned} \tag{10}$$

where $\rho_s$ is the bulk density of the solid phase and $\rho_f$ the density of the pore fluid.

## Model 2 - Hydrate is part of the solid

In this case, we assume that hydrate becomes part of the solid sediment frame. This has two effects: porosity reduction and a change in the elastic frame moduli. The reduced porosity $\phi_r$ can be expressed as:

$$\phi_r = \phi\,(1 - S_h), \tag{11}$$

where $S_h$ is the hydrate saturation of the pore space.
The bulk and shear moduli of the solid phase are now a mixture of the sediment solid and the hydrate. The Hill average is proposed as a way to estimate the effective moduli:

$$\begin{aligned} K &= \frac{1}{2}(f_h\, K_h + (1-f_h)\, K_s + [f_h/K_h + (1-f_h)/K_s]^{-1}), \\ G &= \frac{1}{2}(f_h\, G_h + (1-f_h)\, G_s + [f_h/G_h + (1-f_h)/G_s]^{-1}), \end{aligned} \tag{12}$$

where $K_s$ and $G_s$ are the bulk and shear moduli of the sediment without hydrate and $f_h$ is the volume fraction of hydrate in the solid phase, calculated as:

$$f_h = \frac{\phi\, S_h}{1 - \phi\,(1 - S_h)}. \tag{13}$$

The dry and saturated moduli and the velocities can then be determined using equations 8, 9 and 10.

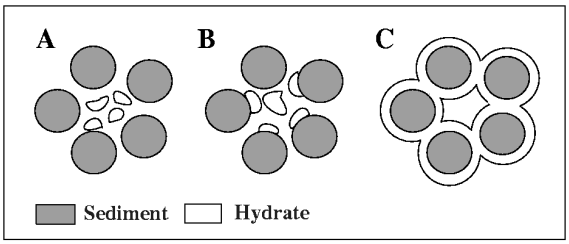


Figure 2: Hydrate inclusion models discussed in Ecker et al. (1997). In model A, the hydrate is part of the pore fluid, in model B the hydrate is part of the solid frame, and in model C the hydrate cements the grain contacts. [**NR**]

# 3D FORWARD MODELING OF SEVEN-COMPONENT DATA

## Modeling setup

The purpose of our forward modeling was to synthesize ocean-bottom seismic acquisition, therefore we used a simple 2-layer model of water over solid. The source was at the water surface, and receivers were at the water bottom. There was a near-seabed anomaly included in the model. The anomaly generated scattering of both P- and S-waves, which upon interacting with the seabed also gave rise to seabed interface waves, termed Scholte waves.

The modeling geometry is shown in Figure 3. Inline and crossline sections going through the center of the anomaly of the $V_p$ and $V_s$ velocity models are shown in Figures 4(a) and 4(b). The parameters of the two layers were:

1. $V_{p1} = 1.5\,\mathrm{km/s},\ V_{p2} = 1.7\,\mathrm{km/s}.$
2. $V_{s1} = 0\,\mathrm{km/s},\ V_{s2} = 0.6\,\mathrm{km/s}.$
3. $\rho_1 = 1.025\,\mathrm{gr/cm^3},\ \rho_2 = 2.0\,\mathrm{gr/cm^3}.$

The anomaly was a Gaussian, which extended outward to a radius of 10 meters, and was centered 10 meters below the seabed. The medium parameters at the center of the anomaly were $V_p = 1.85\,\mathrm{km/s}$, $V_s = 0.9\,\mathrm{kms}$, and $\rho = 2.4\,\mathrm{gr/cm^3}$. Its coordinates were $Y = 50m, X = 150m$. The near-seabed anomaly simulates a "rock" buried just below the seabed, or the leg of a platform, either of which could be sources for scattered interface waves.

The source was a pressure source simulating an airgun, located along the water surface at $Y = 50m, X = 50m$. The wavelet was a Ricker with 25Hz central frequency. There is no source-side ghost from the water surface, since we used an absorbing upper boundary. However, this ghost is simulated by the second lobe of the injected Ricker

wavelet. The lower boundary was rigid, simulating a flat reflector with a reflection coefficient of 1. This rigid lower boundary generated body wave reflections.

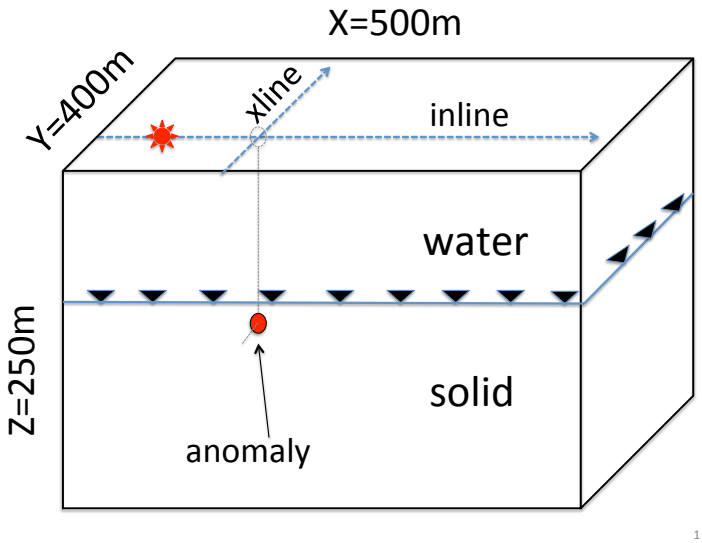


Figure 3: Arrangement of forward modeling. Receivers are on the sea bed, at a depth of 100m. The red star indicates the source position. The red circle indicates the anomaly position. The dashed lines indicate the inline and crossline coordinates along which later sections are displayed. The anomaly is inline with the source. Absorbing boundaries were used everywhere except for the bottom boundary, which was rigid. This simulated a flat reflector with a reflection coefficient of 1. [**NR**]

## Synthetic data

The following Figures 5-11(b) show the seven components of the recorded data. The particle-velocity figures are all scaled identically, and therefore the amplitudes are comparable between figures. The same is true for the rotational data figures.

Figure 5 is the hydrophone section, centered on the coordinates of the anomaly. The inline section is along a line connecting the pressure source and the anomaly center (see Figure 3). Some of the arrivals are annotated. "P1" is the first P reflection off the bottom rigid boundary. Two more P reflections off the same boundary can be seen at later times. "SV1" is the first S wave reflection off the bottom boundary. A faint Scholte wave can be observed as well. Most of the pressure is due to the P-waves, yet the other waves still transmit some pressure into the water column as a result of using a "hard" water bottom in the synthetic modeling, instead of a more realistic velocity/density gradient that generally exists in the shallow subsurface.

Figures 6(a) and 6(b) are the inline and crossline sections of the $v_z$ component. The Scholte wave is relatively strong on this component in both propagation directions.

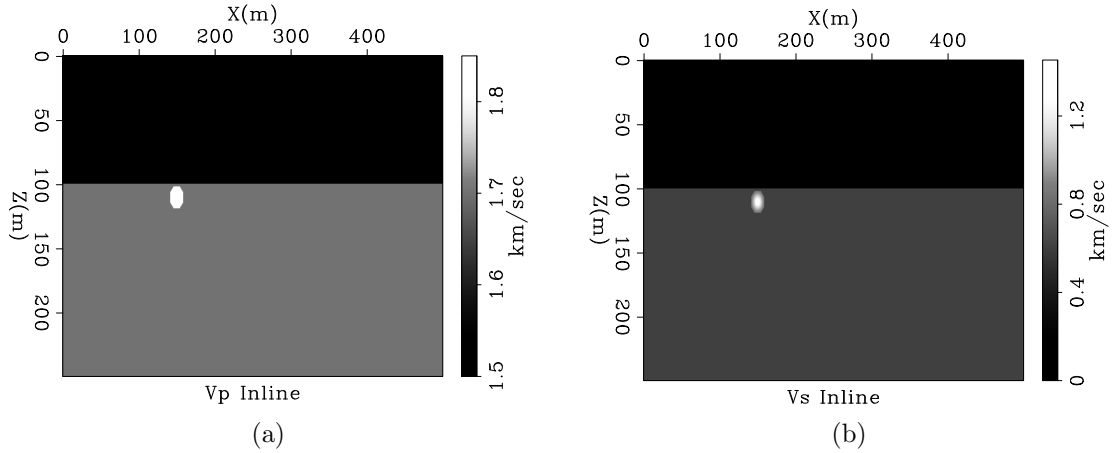


Figure 4: Velocity models. (a) Inline $V_p$ velocity model going through center of anomaly. (b). Inline $V_s$ velocity model going through center of anomaly. The anomaly is a Gaussian, with a radius of 10 meters. [**ER**]

However, on the inline $v_x$ component shown in Figure 7(a), the Scholte wave is weaker. This is a result of the incidence angle of the direct wave on the anomaly ( $45^o$). The Scholte wave is propagating at about 90% of the shear-wave velocity in the medium.

Figure 7(b) is the $v_x$ component in the crossline direction. Here we do not observe a Scholte wave. Rather, we see "SH1", a horizontally polarized shear wave that was generated by the direct wave's scattering off the anomaly in the crossline direction. This wave propagates at shear-wave velocity, just slightly faster than the Scholte wave. There is also "SH2", which is similarly horizontally polarized. This scattering is generated by the body SV reflection, but seems to have a hyperbolic moveout and not a linear moveout typical of a surface wave.

Figure 8(a) should ideally not show any energy, however some energy is still visible. This is due to the numerical approximation of the finite difference scheme, and also the result of using a staggered grid. We do observe particle velocity $v_y$ in the crossline section in Figure 8(b). Most of it is due to the body waves, but there is some Y-motion resulting from Scholte waves scattering in the crossline direction.

Figure 9(a) is the rotation around the Y-axis ($r_y$, or pitch) in the inline direction. Note the prominence of the Scholte wave in this section versus Figures 6(a) and 7(a). This suggests that the Scholte wave has a relatively stronger rotational versus linear component than does the P-wave. This agrees with the retrograde elliptical motion of Scholte waves, which causes a greater rotational deformation in the medium than do body waves. Note also the prominence of the rotation generated by the SV wave. It is evident that all wave modes generate pitch motion. This is due to the fact that the measurement surface is effectively a discontinuity in the medium (solid $\rightarrow$ fluid). Therefore even an incident P-wave causes the surface to tilt slightly, and generate a reading in the rotation sensor.

In the crossline direction of the pitch component in Figure 9(b), only the body waves should be visible, since the source is offset in the inline direction away from the observed crossline. There is still some scattered energy visible, however, and we attribute this again to the staggered-grid, and also to the fact that near the scatterer the wavefield is highly curved. The same reasoning explains why we see roll ($r_x$) energy in the inline direction in Figure 10(a), where none should ideally exist. Such energy implies a wave that is corkscrewing in the direction of its propagation.

Figure 10(b) shows the roll ($r_x$) component in the crossline direction. Here both the body waves and the Scholte waves scattered in the crossline direction are distinguishable. Also visible are two linear artifacts marked "A1" and "A2". These artifacts are the result of the absorbing boundaries generating a rotational motion in the wavefield.

Figure 11(a) is the rotation around the Z-axis ($r_z$, or yaw) in the inline direction. Note the nearly zero energy in the section. This is because none of the waves present in this direction, i.e., P, SV and Scholte, generate a horizontal deformation on the sea bottom. However, in the crossline direction in Figure 11(b) we can see scattered waves "SH1" and "SH2", visible also in the crossline $v_x$ section in Figure 7(b). These waves are not Scholte waves, but rather SH waves propagating at shear velocity. They are picked up only by the vertical rotation component, since they are the only ones that can generate a horizontal deformation on the measurement surface. Also visible are the two artifacts "A1" and "A2" generated by the presence of the absorbing boundary.

## Singular value decomposition of arrivals

The seven component data comprises data of different units and different amplitude ranges. To use SVD in a meaningful way, we first normalized the pressure component, the particle-velocity components and the rotational-motion components separately. Each component type (pressure, linear motion, rotational motion) was normalized by the maximum value within that component. We then applied SVD to time windows taken around the arrivals annotated in Figures 6(a)-11(b). The purpose was to have just one arrival within each time window, but as a result of multiple events and artifacts this was not always the case.

Figures 12(a)-13(d) show the first two polarization vectors for each arrival, scaled by the respective first two singular value (i.e. $s_1$ and $s_2$ of equation 6). Most of the amplitude of the arrivals resides in these two polarization directions. Figure 12(a) shows the polarization of the P-wave arrival in the inline direction. ("P1" in Figure 6(a)). Note how the particle-velocity $v_z$ and pressure component $H$ are dominant, but we also see that the pitch ($r_y$) component is strong, too. This P arrival is as at a near offset, so most of the linear motion should be in $Z$. The rotational motion is a result of the P-wave impinging on the water-bottom discontinuity at an angle, causing the surface to tilt slightly.

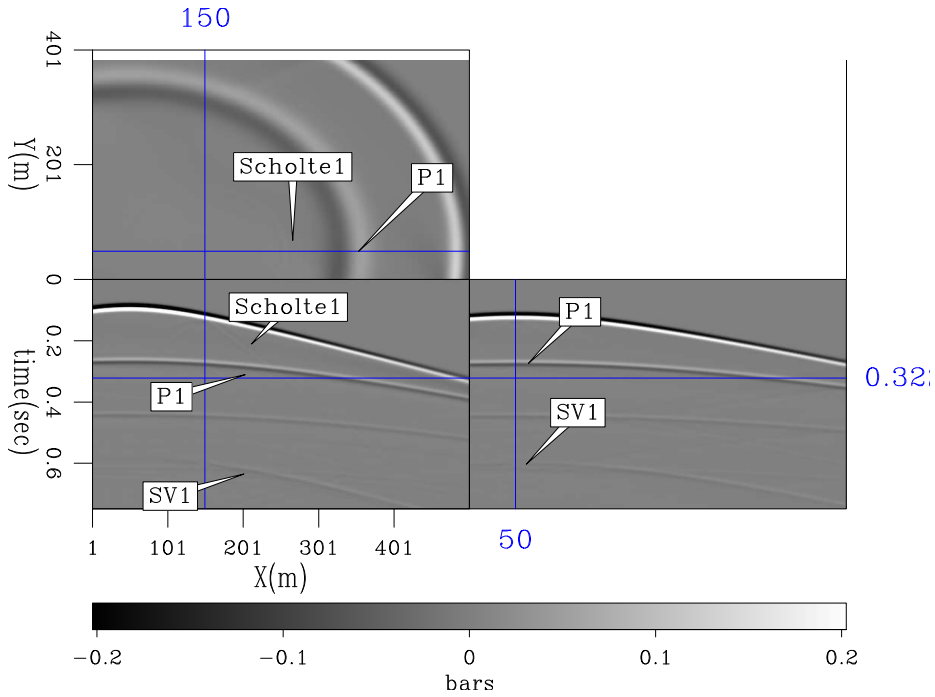


Figure 5: Pressure recorded at the sea bed along inline, crossline and time-slice. The inline and crossline sections are centered on the anomaly coordinates. Some of the arrival time windows where SVD is applied are annotated. Note that most of the pressure is due to P-waves, yet all wave types transmit some pressure into the water column as a result of using a "hard" water bottom in the synthetic modeling. Note also the faint appearance of the Scholte wave. [**CR**]

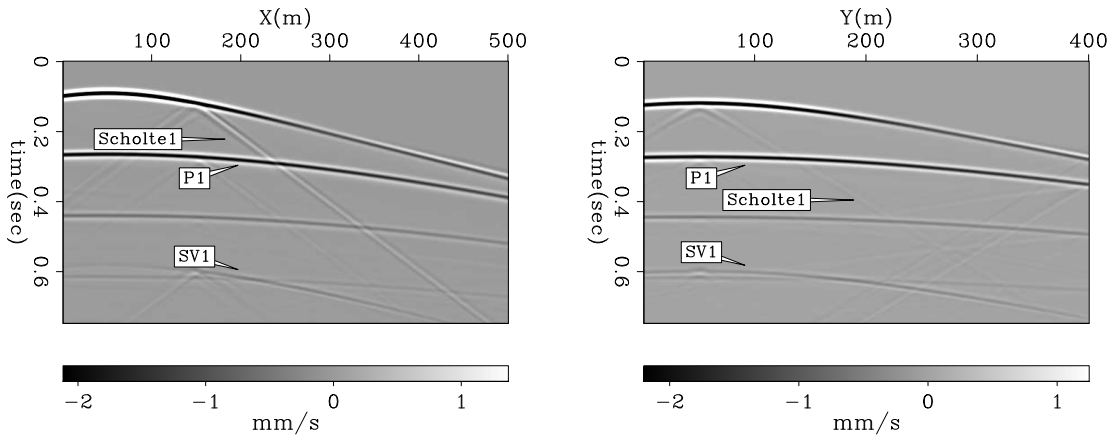


Figure 6: Vertical particle velocity ($v_z$) recorded at sea bed. (a) Inline direction at y=50m. (b) Crossline direction at x=150m. Some of the arrival time windows where we applied SVD are annotated. "Scholte1" is generated by the direct arrival hitting the anomaly. "P1" is the first P reflection off the bottom rigid boundary. Another two P reflections off the same boundary can be seen at later times. "SV1" is the first S wave reflection off the bottom boundary. Each body wave arrival generates some scattered Scholte wave when it hits the anomaly. [**CR**]

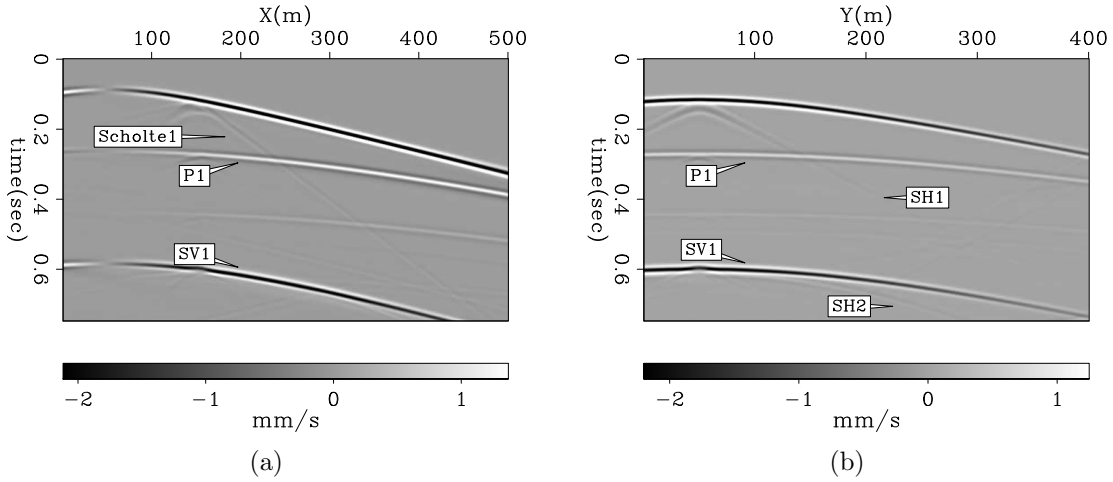


Figure 7: Horizontal particle velocity in X direction ($v_x$) recorded at sea bed. (a) Inline direction at y=50m. (b) Crossline direction at x=150m. [**CR**]

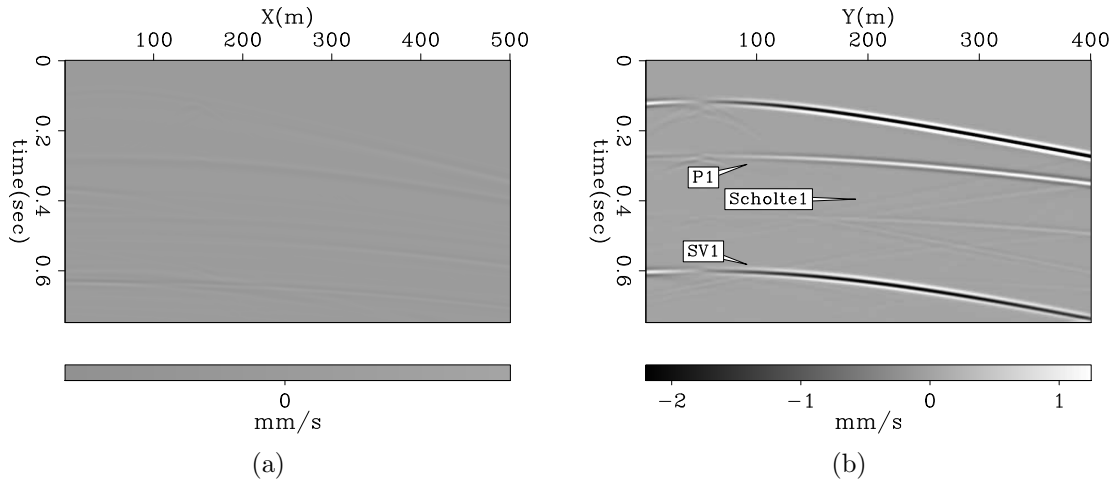


Figure 8: Horizontal particle velocity in Y direction ($v_y$) recorded at sea bed. (a) Inline direction at y=50m. (b) Crossline direction at x=150m. [**CR**]

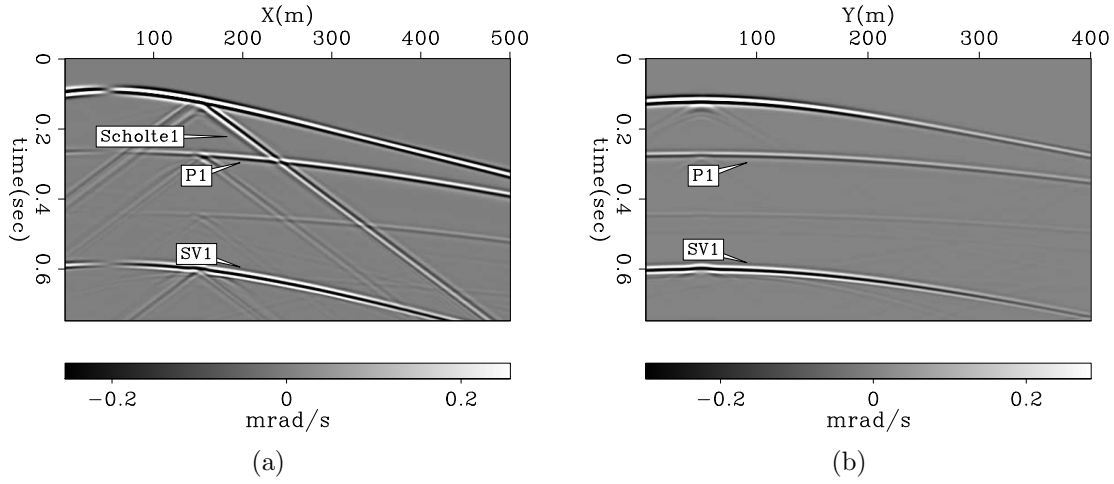


Figure 9: Horizontal particle rotation around Y-axis ($r_y$, pitch) recorded at sea bed. (a) Inline direction at y=50m. (b) Crossline direction at x=150m. [**CR**]

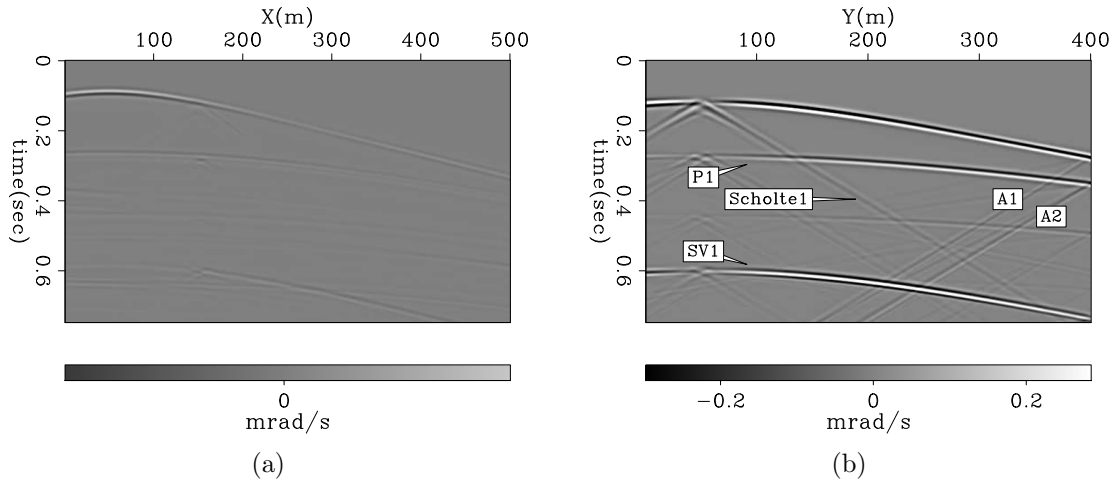


Figure 10: Horizontal particle rotation around X-axis ($r_x$, roll) recorded at sea bed. (a) Inline direction at y=50m. (b) Crossline direction at x=150m. [**CR**]

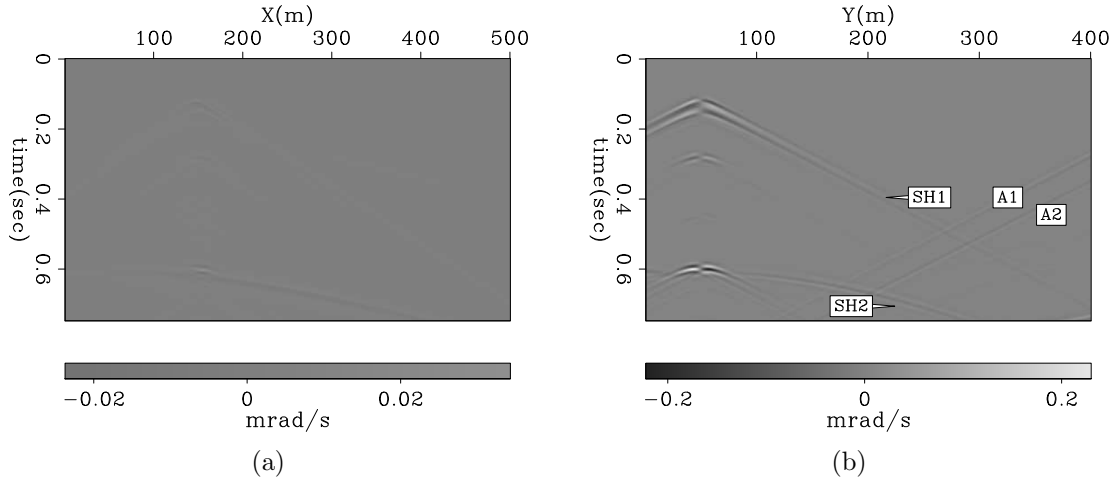


Figure 11: Vertical rotation around Z-axis ($r_z$, yaw) recorded at sea bed. (a) Inline direction at y=50m. (b) Crossline direction at x=150m. [**CR**]

Figure 12(b) shows the polarization of the SV arrival in the inline direction. There is a large rotational component in the $r_y$ direction, while in the linear direction the $v_x$ component is dominant. This S arrival is at the same offset as the P arrival, therefore we can expect most of the linear motion to be in the $X$ direction.

The polarization of the inline Scholte wave is shown in 12(c). Note how the rotational motion is the dominant component here.

Figure 13(a) is again a P-wave arrival, but along the crossline direction (see Figure 3), and at an inline offset from the source position. Therefore it is reasonable that it is polarized linearly in all directions. It also explains why this arrival is also polarized in both $r_x$ and $r_y$ directions.

Figure 13(b) is the SV arrival at the same ocean-bottom location as Figure 13(a). It is polarized in the linear $v_x$ and $v_y$ directions, and in the rotational $r_x$ and $r_y$ directions. This polarization is consistent with this waves propagation direction at this particular location.

Figure 13(c) is the Scholte wave in the crossline direction. Unlike Figures 13(a) and 13(b), this arrival is only offset from its source, the sea-bottom anomaly, in the crossline direction. Therefore it is polarized in the $r_x$ direction only.

Figure 13(d) is an SH wave ("SH2" in Figure 11(b)). It is the result of scattering off the anomaly. This arrival is taken from an offset in both the crossline and inline direction from the anomaly. The dominant polarization direction is in the $r_z$ direction. We also see that it is polarized in the linear $v_x$ direction. Upon closer inspection of this arrival, we saw that the chosen time window also contains some P-wave energy and some of a boundary-generated artifact. This is the reason for the strong $r_x$ polarization.

Observing all these figures, we can arrive at guidelines for identifying the arrival type from the polarization vectors:

1. P-waves are polarized in the hydrophone direction, but mostly in the linear motion components' directions. They have a lesser polarization in one or two horizontal rotation directions.

2. SV waves are polarized largely in the horizontal rotational-motion direction, but also have a significant polarization in one or two linear-motion directions.

3. Scholte wave polarization is predominantly in the horizontal-rotation directions.

4. SH waves are unique in their polarization direction in the vertical-rotation direction. They also have a significant polarization in one or two linear-motion directions.

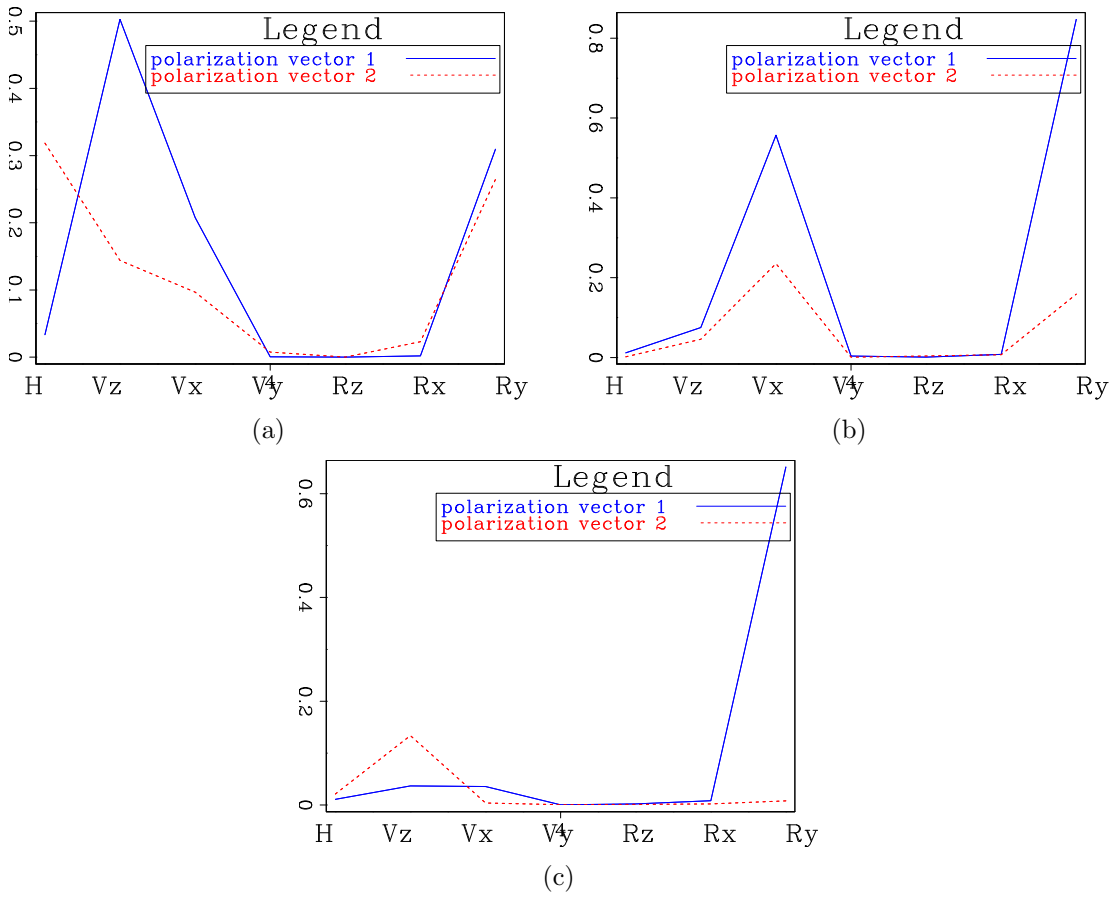


Figure 12: The first two polarization vectors resulting from application of SVD to the seven components of the arrivals annotated in Figure 6(a) at the ocean-bottom receiver at $x = 200, y = 50$. The vector components are along the X-axis, and the Y-axis shows the magnitude of the vector along each component. (a) Inline reflected P-wave arrival ("P1" in Figure 6(a)). (b) Inline reflected SV wave arrival ("SV1"). (c) Inline scattered Scholte wave ("Scholte1"). The units on the Y-axis are amplitudes of the vector components within each arrival's time window. The P-wave is polarized mostly in the $v_z$ axis, but also in the hydrophone and $r_y$ axes. The SV wave is polarized mostly in the $r_y$ and $v_x$ axes. The Scholte wave is polarized almost entirely in the $r_y$ direction. [**CR**]

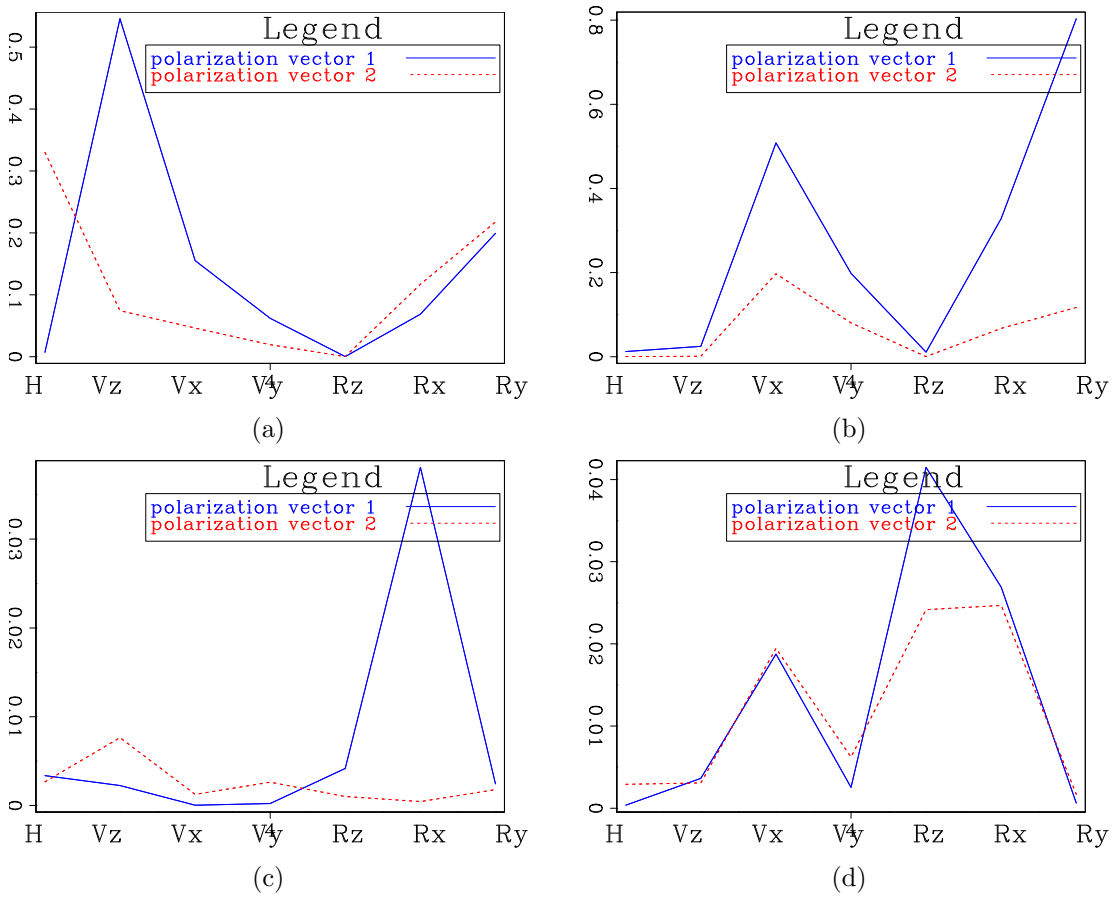


Figure 13: The first two polarization vectors resulting from application of SVD to the seven components of the arrivals annotated in Figure 6(b). The vector components are along the X-axis, and the Y-axis shows the magnitude of the vector along each component. (a) Crossline reflected P-wave arrival at $x = 150, y = 90$ ("P1" in Figure 6(b)). (b) Crossline reflected SV wave arrival at $x = 150, y = 90$ ("SV1"). (c) Crossline scattered Scholte wave at $x = 150, y = 212$ ("Scholte1"). (d) Crossline scattered SH wave at $x = 280, y = 230$ ("SH2" in Figure 11(b)) The units on the Y-axis are amplitudes of the vector components within each arrival's time window. The P-wave is polarized mostly in the $v_z$ and $v_x$ axes, but also in the hydrophone and $r_y$ and $r_x$ axes. The SV wave is polarized mostly in the $r_y$ and $v_x$ axes, but also in the $v_y$ and $r_x$ axes. The Scholte wave is polarized almost entirely in the $r_x$ direction. The SH wave is polarized in the $r_z$ direction, and also in the $r_x$ and $v_x$ directions. [**CR**]

## AVO OF 2D ROTATIONAL DATA

For the mineralogy, porosity and hydrate saturation of the medium near the Blake Outer Ridge, we used the values estimated by Ecker et al. (1997). We then used equations 8-13 to generate two effective elastic media, one for the "hydrate as fluid" model and one for the "hydrate as solid" model.

The media had three layers: A water layer, a water-saturated sediment, and a hydrate saturated sediment. The only difference between the media was the inclusion model, and therefore the only difference between the models was in the $V_p$, $V_s$ and density of the hydrate layer. The models are shown in Figures 14(a)-14(d).

We synthesized OBS data with these models, and generated CMP gathers for one surface location. We used flat layers only, therefore the amplitudes in these CMP gather approximate those of a basic AVO done in surface coordinates. The gathers were of the hydrophone component and of the $r_y$ component. The wave-propagation was done in two dimensions only, therefore the only rotational component is around the Y axis.

In Figures 15(a)-15(f) we show the PP and the PS reflections from the top of the hydrate layer. All Figures are of the same CMP location, and the maximum reflection angle present in the gathers is $40^o$. Figure 15(a) is the hydrophone CMP gather for hydrate model 1, and Figure 15(b) is the $r_y$ CMP gather for the same model. Note how the $r_y$ component shows a stronger converted-wave response than the hydrophone, and records very little of the primary P-wave by comparison.

Figures 15(c) and 15(d) are the hydrophone and $r_y$ components for hydrate inclusion model 2. In this case the hydrate is part of the solid, resulting in an increase of the bulk modulus. This increases the P-wave reflectivity, and therefore the amplitude of the PP reflection in the hydrophone component. However, the shear modulus is relatively more affected by the change, and therefore the PS reflection's amplitude increases by a greater factor. Note how this change in shear modulus is more significant on the $r_y$ component than on the hydrophone component.

Figures 15(c) and 15(f) are the differences in reflection amplitudes with offset between the two hydrate models. The hydrophone component does vary with the change in inclusion model, however note how the $r_y$ component exhibits much more sensitivity to the same change, especially at the shorter offsets.

## DISCUSSION AND CONCLUSION

We have applied SVD as a method to ascertain the motion components of discrete arrivals. We have shown that different wave-types have different signatures when observing their scaled polarization vectors after applying SVD to the multicomponent data. The rotation data provide additional information about the motion components, and by inference they provide an indication as to the wave type recorded by

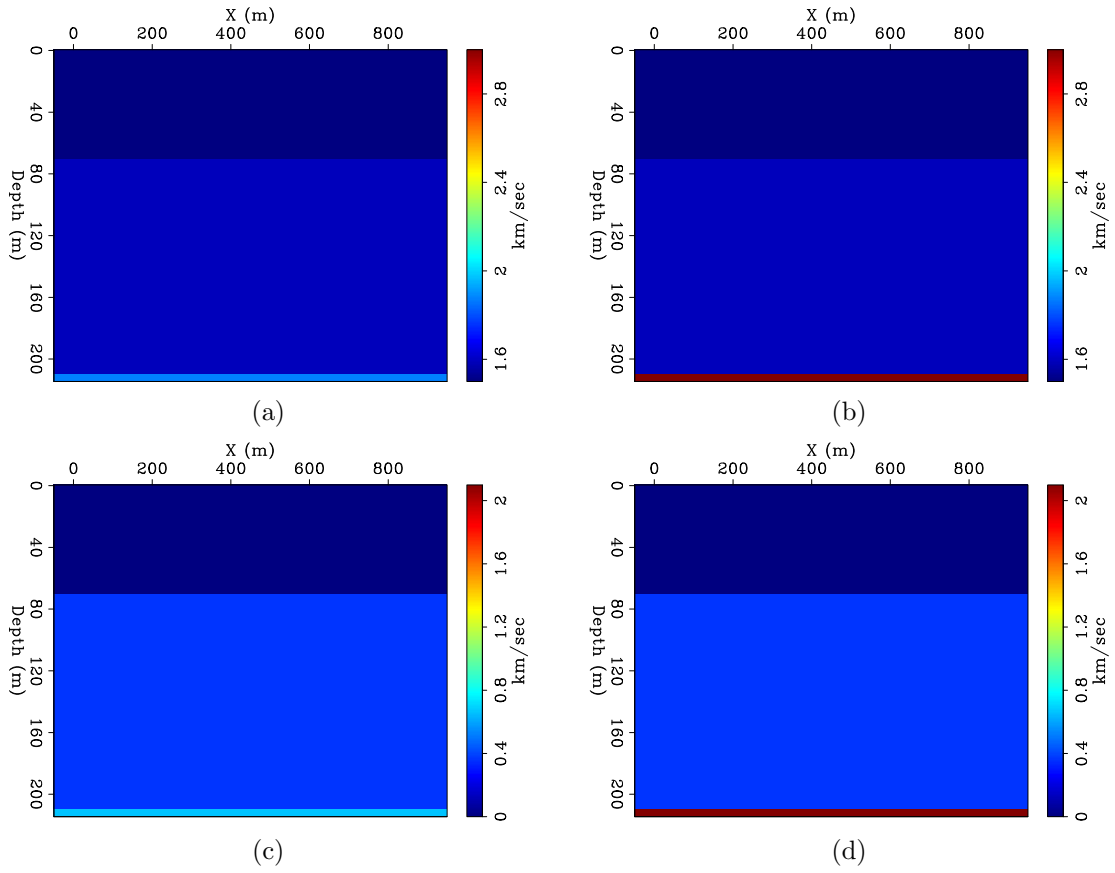


Figure 14: $V_p$ and $V_s$ models resulting from the two hydrate inclusion models. The hydrate layer is at $z = 207$m, and it is only in that layer that the models differ. (a) $V_p$ of hydrate inclusion model 1, hydrate velocity is 1.87km/s. (b) $V_p$ of hydrate inclusion model 2, hydrate velocity is 3km/s. (c) $V_s$ of hydrate inclusion model 1, hydrate velocity is 0.66km/s. (d) $V_s$ of hydrate inclusion model 2, hydrate velocity is 2.1km/s. [**ER**]

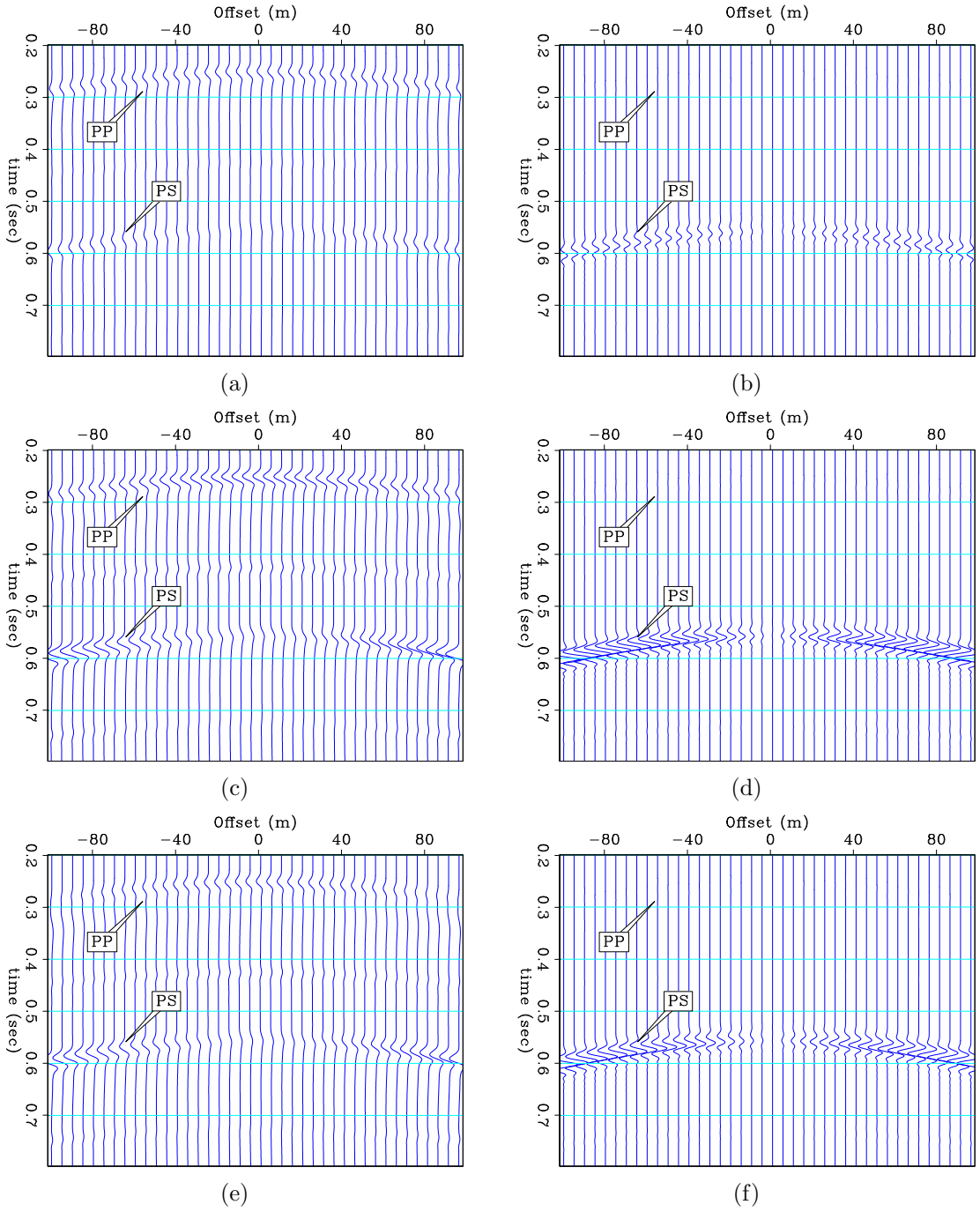


Figure 15: A CMP gather from the two hydrate models, showing the PP and the PS reflections from the top of the hydrate layer as they appear on the hydrophone and the rotational $r_y$ (pitch) component. (a) Hydrophone, hydrate model 1. (b) $r_y$, hydrate model 1. (c) Hydrophone, hydrate model 2. (d) $r_y$, hydrate model 2. (e) Hydrophone response difference. (d) $r_y$ response difference. The rotational $r_y$ component's AVO is evidently more sensitive to the change in hydrate inclusion model than is the hydrophone. [**CR**]

ocean-bottom acquisition.

We have shown that interface waves have a predominantly rotational signature. Shear waves also have a large rotational component, however they also exhibit a stronger linear polarization than the interface waves. P-waves have a mostly linear polarization, although they do have some rotational-motion component. The P-waves are unique in having a significant polarization in the hydrophone "direction".

We have also shown that it is possible to distinguish between SV and SH waves by observing the amplitude of their $r_z$ polarization versus their $r_x$ or $r_y$ polarizations. It is interesting to note that the only waves missing in the vertical rotation section (Figure 11(b) are the P and SV body waves. This suggests an interesting application for a vertical rotation sensor: selection of SH or of Love waves.

The advantage of having this information is that we do not need to rely on a good spatial sampling of the data in order to identify and separate the wave-types by their moveouts/wavenumbers. This is particularly relevant for surface waves, since they propagate at much lower velocities than body waves, and are likely to be aliased in the data.

There are as yet some unresolved issues in regard to SVD of seven-component data:

1. Scaling between hydrophones, geophones and rotation sensors. Each type of sensor measures a different unit, and it is the relation between the amplitudes of the different components that will determine the polarization vectors. Even if there is a lot of surface wave energy in a particular arrival, the recorded rotational-motion values must be scaled accordingly such that they won't be too small compared to the linear components.

   In this synthetic example, the entire dataset had ample amounts of each motion component, and therefore normalizing the hydrophone, geophones and rotation sensors separately was successful. However, for field data the question of how to scale each of the components is not trivial. It is reasonable to assume that the greatest amplitude of the vertical geophone corresponds to greatest amplitude of the pressure (the direct wave propagating vertically from the source to the geophone directly beneath it on the seabed). However, it is not so intuitive to see where the greatest value of rotation should be, and therefore the scaling between geophone and rotation sensors remains an open question at this point.

2. We have shown a noise-free synthetic. How will noise affect the SVD result in field data? How much noise is required in order for the particular signatures of each arrival to not be obvious? Will noise be equally distributed between the linear and rotational components?

We have also shown that rotational data can provide us with better constraints for rock-physics models. In this case, the change in the rock-physics model had a

significant effect on the shear modulus of gas hydrate, and therefore on the shear-wave reflectivity. Since the reflected S wave generates a greater rotation on the ocean-bottom than the P-wave, the $r_y$ sensor provides us with a proxy for the shear-wave reflectivity. We can use this proxy to construct AVO from seismic data, and validate our hydrate inclusion model (given some known rock-properties of the medium).

## ACKNOWLEDGEMENTS

We thank Tim Owen, Malcolm Lansley and Bob Brune for prompting us to consider rotation sensors, Fred Herkenhoff for showing us rotational field data from Chevron's recent experiment, and John Evans from USGS.

## REFERENCES

Brokesova, J. and J. Malek, 2010: 2nd IWGoRS Workshop in Prague.

Brune, R., D. Aldridge, M. van der Baan, J. Gaiser, and E. Muyzert, 2012, Theta-data: Introduction to rotational seismology and its potential uses: 82nd SEG Conference and Exhibition.

deMeersman, K., M. van der Baan, and J. Kendall, 2006, Signal extraction and automated polarization analysis of multicomponent array data: Bulletin of the Seismological Society of America, **96**, 2415–2430.

Dvorkin, J. and A. Nur, 1993, Rock physics for characterization of gas hydrates: The future of energy gases: USGS Professional Paper 1570, 293–298.

———, 1996, Elasticity of high-porosity sandstones: theory for two north sea datasets: Geophysics, **61**, 1363–1370.

Ecker, C., J. Dvorkin, and A. Nur, 1997, Estimating the amount of gas hydrate and free gas from surface seismic: Stanford Exploration Project, **Report 95**, 173–195.

Edme, P., E. Kragh, and E. Muyzert, 2012, Noise attenuation using rotation data: U.S. Patent application publication, **Pub. No.: US 2012/0250460 A1**.

Lee, W. H. K., H. Igel, and M. D. Trifunac, 2009, Recent advances in rotational seismology: Seismological Research Letters, **3**, 479–490.

Muyzert, E., A. Kashubin, E. Kragh, and P. Edme, 2012, Land seismic data acquisition using rotation sensors: 74th EAGE Conference and Exhibition.

Virieux, J., 1986, P-Sv wave propagation in heterogeneous media: Velocity-stress finite difference method: Geophysics, **51**, 889–901.